An Externally Dispersed Interferometer Prototype for Sensitive Radial Velocimetry: Theory and Demonstration on Sunlight

DAVID J. ERSKINE

Lawrence Livermore National Laboratory, University of California, 7000 East Avenue, Livermore, CA 94550-9234; erskine1@llnl.gov

ABSTRACT. A theory of operation of a wideband interferometric Doppler spectroscopy technique, called externally dispersed interferometry (EDI), is presented. The first EDI prototype was tested on sunlight and detected the 12 m s^{-1} amplitude lunar signature in Earth's motion. The hybrid instrument is an undispersed Michelson interferometer having a fixed delay of about 1 cm, in series with an external spectrograph of about 20,000 resolution. The Michelson provides the Doppler shift discrimination, while the external spectrograph boosts net white-light fringe visibility by reducing cross talk from adjacent continuum channels. A moiré effect between the sinusoidal interferometer transmission and the input spectrum heterodynes high spectral details to broad moiré patterns, which carry the Doppler information in its phase. These broad patterns survive the blurring of the spectrograph, which can have several times lower resolution than grating-only spectrographs typically used now for the Doppler planet search. This enables the net instrument to be dramatically smaller in size (∼1 m) and cost. The EDI behavior is compared and contrasted to the conventional grating-only technique.

1. INTRODUCTION

The search for extrasolar planets through the Doppler effect in light from the parent star is one of the most exciting aspects of astronomy today (Marcy & Butler 2000; Cumming, Marcy, & Butler 1999). The current Doppler technique requires a high-resolution grating spectrometer (e.g., Vogt et al. 1994; Mayor & Queloz 1995; Marcy & Butler 1996; Butler et al. 1996; Noyes et al. 1997; Cochran et al. 1997; Vogt et al. 2000). The minimum typical line width of absorption-line features in stellar and solar spectra at 5000–6000 Å is ∼0.1 Å, about 5–6 km s^{-1} in equivalent Doppler velocity. Hence, a grating resolution ($R \equiv \lambda/\Delta\lambda$) of 60,000 or larger is required. The high spectral resolution forces large diameter optics to be separated by long distances (5 and 7 m scales of the Keck and Lick Observatory spectrometers [Vogt 1987; Vogt et al. 1994], respectively). To achieve optical stability, the components must be mounted on heavy support structures that can cost millions of dollars in construction expense.

Interferometers with fixed delays have been used previously to measure precision (∼3 m s^{-1}) Doppler velocities in solar physics, but these have been narrowband devices observing a single absorption line (Title & Ramsey 1980; Harvey et al. 1995; Kozhevatov, Kulikova, & Cheragin 1996). Consequently, only a small fraction of incident flux is used, restricting their application to bright sources.

We introduce a hybrid approach (Erskine 2000, 2002; Erskine & Ge 2000; Ge 2002; Ge, Erskine, & Rushford 2002) to high-resolution spectroscopy that combines interferometry and multichannel dispersive spectroscopy and has unlimited bandwidth

not seen in prior hybrid instruments, along with other practical advantages common to interferometers. These include small size (∼1 m), low cost, high etendue (solid angle × area), and potential high efficiency. We call it an externally dispersed interferometer (EDI). An undispersed Michelson interferometer (to provide Doppler sensitivity) is placed in series with an external grating spectrograph (to suppress the cross talk of the continuum; Fig. 1).

A fringing spectrum is produced on the CCD of the external spectrograph. The Doppler effect shifts the fringe phase for each absorption line. Since these shifts are nearly the same over the entire bandwidth, they can be averaged together to produce a strong net signal, in spite of a lower resolution disperser. The lower grating resolution in turn allows for much smaller and inexpensive instruments.

Furthermore, the interferometer spectral comb imprinted on the beam acts as a fiducial that is carried wherever the beam goes inside the spectrograph. Changes in the spectrograph point-spread function (PSF) affect the comb the same way as the input spectrum, reducing the velocity errors due to PSF drifts.

1.1. Comparison to Previous Hybrids

Prior demonstrations of cross-dispersed interferometry differ from our EDI method in important ways. Born & Wolf (1980, pp. 333–338) and McMillan et al. (1993) describe a Fabry-Perot interferometer cross-dispersed with a spectrograph to separate the orders. However, this Fabry-Perot, having high finesse, does not produce sinusoidal fringes, and therefore the
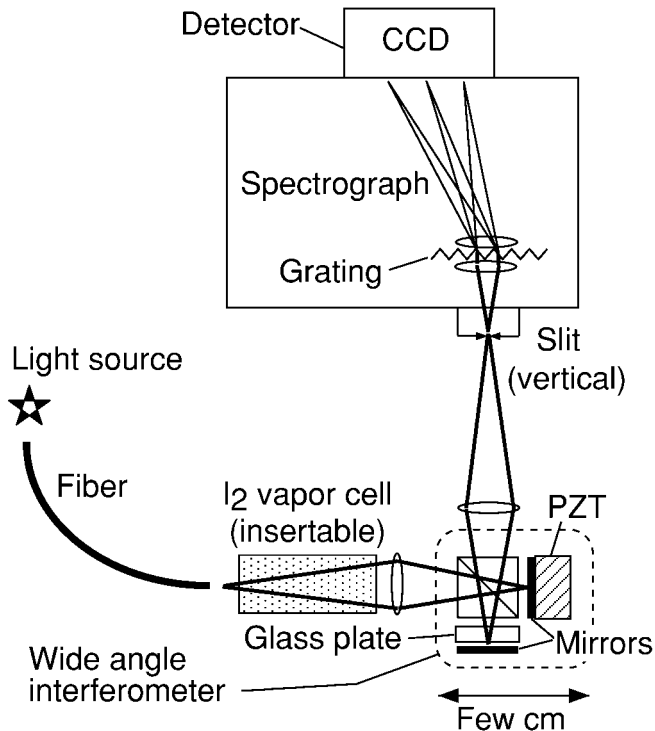
FIG. 1.—Schematic of the EDI: Sunlight from a roof-mounted heliostat conducted through fiber leads to an iodine vapor cell that provides a reference spectrum. The wide-angle interferometer with an 11 mm fixed delay created by a glass plate imprints the fringes on a beam at the spectrograph slit, creating a fringing spectrum at CCD. The PZT transducer steps the interferometer delay in four quarter-wave increments, to remove nonfringing artifacts in multiple exposures. The Jobin-Yvon HR640 grating spectrograph (0.7 m length) with $R \sim 20,000$ disperses light into a 130 Å bandwidth at 5130 Å.
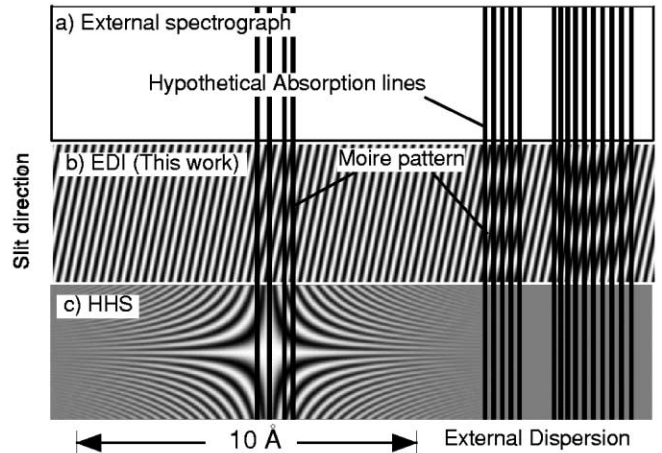

FIG. 2.—Comparison of three different techniques, each recording a hypothetical white-light continuum having a few narrow absorption lines. Blurring is neglected. (*a*) Conventional grating spectrograph. (*b*) In the EDI, both transverse and horizontal periods of the interferometer spectral comb are relatively uniform, allowing use of full bandwidth. (*c*) The HHS uses a grating internal to the interferometer. Changing ray paths limit the effective bandwidth.

1.2. Demonstrations of EDI

We present the first demonstration of the EDI technique to detect an astronomical body, in this case the Earth's Moon, by detecting its 12 m s^{-1} amplitude Doppler signature in the solar spectrum over a 1 month observation. This confirms that the effect measured by the instrument is indeed a Doppler velocity, since the measured and predicted velocities follow each other through 400 m s^{-1} of change as a result of the Earth's rotation (across 5 hr) and eccentric orbit. This also demonstrated that the long-term drifts were low enough, even for an immature prototype, to be useful in detecting many planetary Doppler
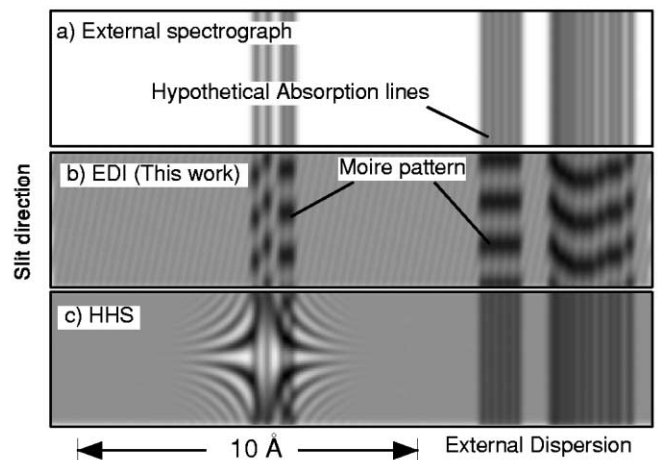
advantages of trigonometry (Fourier analysis and three- or four-exposure phase-stepping algorithms) that come from use of a Michelson cannot be employed to determine precision phase shifts. The spikelike transmission spectrum passes less flux than the sinusoidal Michelson. In the Heterodyned Holographic Spectrograph (HHS; e.g., Douglas 1997; Frandsen, Douglas, & Butcher 1993) and Spatially Heterodyning Spectrometer (e.g., Harlander, Reynold, & Roesler 1992), a grating is incorporated inside the interferometer (as well as externally). This severely limits the bandwidth because different wavelengths combine in a range of angles at the interferometer output to produce widely changing spatial fringe spacings on the CCD detector (Fig. 2*c*). Only for a narrow range of wavelengths (~10 Å) are the spatial frequencies low enough for the detector to resolve (Fig. 3*c*).

In contrast, in our interferometer, the light recombines at the same angle for all wavelengths. Thus, the interferometer component does not limit the system bandwidth. Stellar fringing spectra have recently been taken over the entire bandwidth of the Lick echelle spectrograph (Erskine & Edelstein 2003a).

FIG. 3.—Blurred version of Fig. 2. (*a*) Unresolved lines. (*b*) The EDI moiré fringes survive the blurring over a wide bandwidth. (*c*) The HHS fringes are resolvable only in a narrow region.
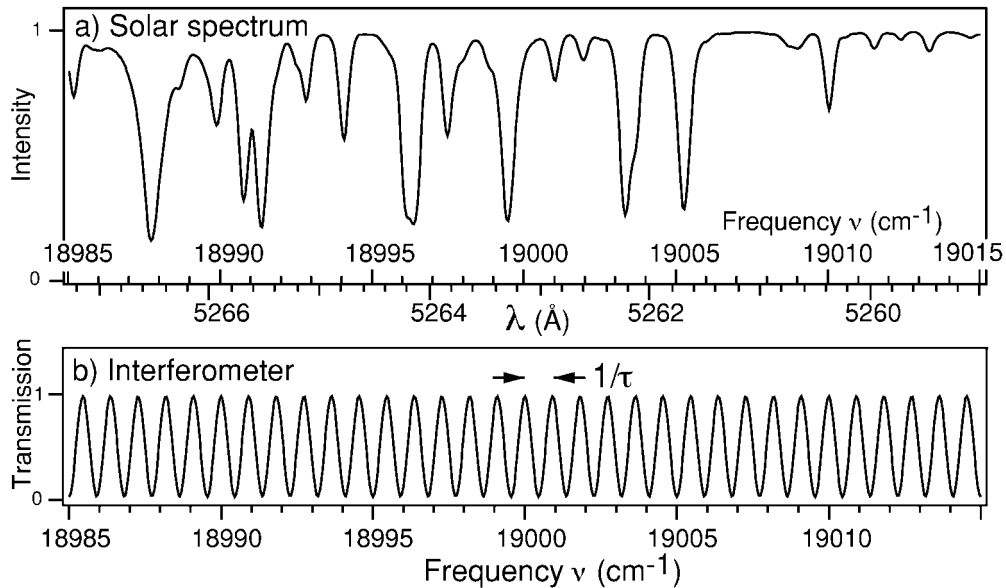
Fɪɢ. 4.—(*a*) Section of the solar spectrum vs. frequency ($\nu = 1/\lambda$, in units of cm^{-1}) or wavelength (λ). (*b*) Sinusoidal transmission function of Michelson interferometer having delay $\tau = 1.1$ cm, for one output arm. This is periodic when plotted vs. ν, making ν the natural dispersion variable. This value of τ yields an interferometer comb peak spacing similar to the typical absorption line width.

signatures. After sunlight demonstrations were performed, the prototype was modified for use at an observatory, and Doppler velocities of bright starlight (Arcturus) were successfully taken at the Lick 1 m telescope (Ge et al. 2002).

2. INTERFEROMETER SPECTRAL COMB

The EDI approach is to use the frequency response $T(\nu)$ of an undispersed Michelson interferometer as the key element to discriminate behavior in the input spectrum. Let the dispersion axis of the external disperser be horizontal and described by frequency and wavelength $\nu \equiv 1/\lambda$. The frequency unit of ν is cm^{-1}. The slit of the external spectrograph sets the transverse or y-direction. The optical path length difference between the two interferometer arms is called the delay (τ), in units of centimeters. The transmission function $T(\nu, y)$ of one interferometer output arm is

$$T(\nu, y) = \tfrac{1}{2}[1 + \gamma \cos (2\pi\tau\nu + \phi_y)],\qquad(1)$$

where ϕ_y is the interferometer phase and γ is the interferometer fringe visibility, which is unity for the ideal situation in which the intensities of the two interfered arms are matched. Figure 4 shows $T(\nu, y)$ for $\tau = 1.1$ cm compared with a section of the solar spectrum.

2.1. Phase Stepping in General

Generally speaking, in order to accurately determine a fringe phase and amplitude, one needs to sample the output intensity

at three or more instances in which τ is dithered slightly. The dither is equivalently described by an interferometer phase

$$\phi_y = 2\pi(\Delta\tau/\lambda).\qquad(2)$$

This process is called phase stepping. A good general discussion can be found in Greivenkamp & Bruning (1992) and references therein. Here phase stepping can be implemented by two independent methods: (1) versus time in multiple exposures, by moving the entire interferometer mirror as a piston using the piezoelectric (PZT) transducer in steps of size $\Delta\phi_p$, and (2) in each exposure simultaneously over all phases, by tilting one mirror relative to the other versus y to create "phase-slanted" fringes having a spatial period P_y along the slit length. The combination of these two is

$$\phi_y = 2\pi(y/P_y) + n\Delta\phi_p,\qquad(3)$$

where n indexes the piston exposures. In practice, we use both methods because that provides excellent discrimination against spurious variations in intensity (such as CCD pixel gain variations) that may mimic fringes. Only true fringes will vary synchronously with ϕ_y as it is dithered both in y and n.

2.2. Phase-slanted Mode

In our predominant style of taking data for a linear spectrograph, one of the interferometer mirrors was tilted vertically so that ϕ varied linearly with y along the slit (phase-slanted). Typically four to six fringe periods were created along the y-

extent of the beam, which was typically 60 pixels tall. Under white-light illumination, this created a fringing spectrum having slanted fringes across the whole bandwidth.

2.3. Phase-Uniform Mode

Alternatively, if the interferometer mirrors are perfectly aligned with each other, then the fringe phase is uniform across the beam and the spatial period infinite. This mode of fringes could be called the "uniform-phase" mode, and the interferometer comb so generated has vertical fringes that depend only on frequency and do not vary transversely to the spectrum.

2.4. Choice of Delay

The delay (τ) is chosen so that the spacing of peaks and valleys in $T(\nu)$ is similar to the typical line widths of absorption lines in the input spectrum. This occurs for $\tau \sim 1$ cm. Figure 4a shows a section of the solar spectrum in the region used for velocimetry, compared with the interferometer spectral comb for $\tau = 1.1$ cm.

The density (ρ) of fringes for $T(\nu)$ along the dispersion axis is equal to τ, which, other than a slight wavelength dependence of the glass delay plate that contributes to τ, is uniform over an extremely wide bandwidth.

3. MOIRÉ FRINGES

Examples of the EDI-measured fringing spectra for sunlight and the reference iodine vapor cell (backlit by white light) are shown in Figure 5. The Jobin-Yvon 640 spectrograph resolution ($R \sim 20,000$) is such that the interferometer spectral comb is only partially seen. The interaction between the comb and the absorption lines produces a moiré pattern. These are the beadlike and smilelike structures seen, respectively, in the solar (Fig. 5a) and iodine (Fig. 5b) data. (Only a small section of the 130 Å bandwidth measured is shown.) These survive the blurring of the spectrograph, whereas the absorption lines themselves may not.

Doppler information is carried in the moiré patterns through their phase shift. These rotate in phase versus the Doppler shift $\Delta\nu_D$ as $e^{i2\pi\tau\Delta\nu_D}$. A novel vector data analysis procedure was developed to precisely measure the differential moiré pattern phase between the input spectrum and the reference (iodine) spectrum, recorded simultaneously in the same fringing spectrum. The phase difference yields the Doppler velocity independent of small changes in τ.

4. SIMPLE MODEL ILLUSTRATING BENEFIT

The reader may understandably be skeptical that the inclusion of interferometer fringes on a spectrum can boost the signal-to-noise ratio (S/N) in measuring a Doppler shift relative to a grating spectrograph used alone. A simple model is presented that demonstrates this in the low-resolution regime, where the intrinsic absorption line is significantly blurred and where the interferometer spectral comb itself cannot be resolved by the spectrograph.
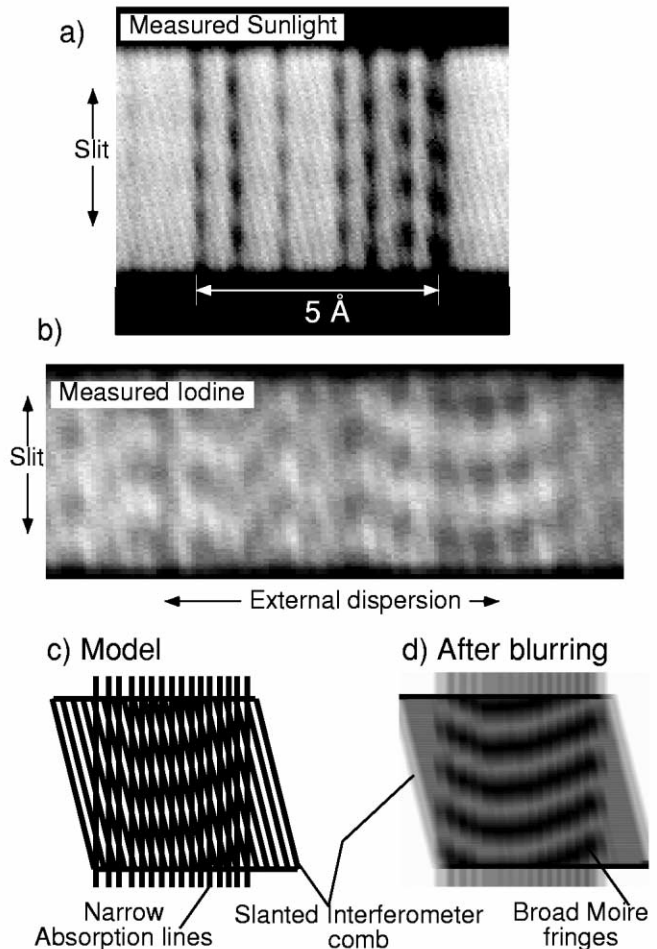

FIG. 5.—(a, b) Snippets of measured solar and iodine fringing spectra taken by the EDI prototype. The full bandwidth was 130 Å. The external spectrograph resolution was sufficiently high ($R \sim 20,000$) to partially resolve the underlying phase-slanted interferometer comb. (c, d) Graphical models explaining formation of "smilelike" moiré pattern seen in iodine data. The high detail spectral features are heterodyned to lower details where they can survive the blurring of the external spectrograph.

For calculational simplicity, the sinusoidal interferometer comb is approximated as a square wave and the intrinsic absorption line as a rectangular well. We further simplify by evaluating only a single interferometer phase, where the absorption line is partially intersecting one of the dark or light fringes. (The actual data-taking configuration samples three or more phases but produces a similar result.)

4.1. Conventional Spectrograph

The steps in calculating the reaction to a Doppler shift on a conventional spectrograph signal are shown in Figure 6. The assumed rectangular intrinsic absorption line in the spectrum $S(\nu)$ having depth H_i and width A_i has an area of H_iA_i. Under blurring, this area is conserved, in $B(\nu)$. Supposing the blurring ratio (A_o/A_i) between observed and intrinsic line widths is large,
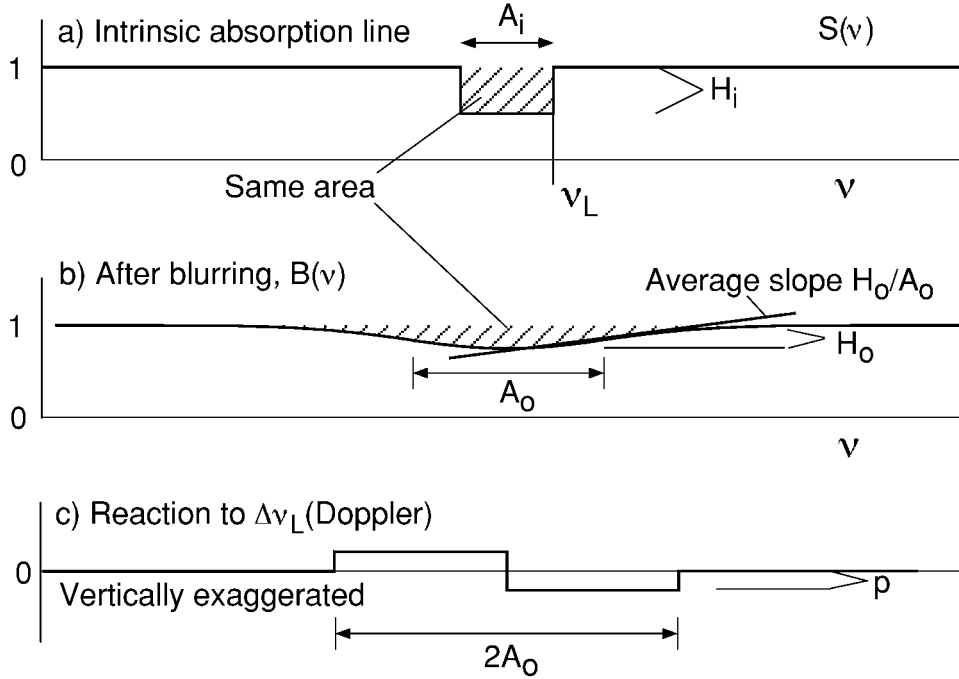
Fig. 6.—Simplified calculation of Doppler reaction function in a conventional spectrograph. (*a*) Intrinsic absorption line modeled as a rectangular well. (*b*) The detected line is blurred to a larger width A_o. The area of the line is conserved under blurring, allowing the calculation of the observed depth H_o. (*c*) The reaction to a shift of the absorption line is approximated by two rectangles.

then the detected line shape is approximately Gaussian or triangular, and the observed depth is $H_o = H_i A_i / A_o$.

The reaction to a Doppler shift $\Delta \nu_D$ in the position ν_L of the absorption line is $\Delta B(\nu) = B(\nu) - B(\nu + \Delta \nu_D)$. Since the average slope of the observed line is H_o/A_o, the reaction function will be two rectangles of modulus $p = (H_o/A_o)\Delta \nu_D$ and width $2A_o$. The signal we seek is the absolute value of the reaction function against the input flux of n photons per wavenumber in the continuum:

$$\text{signal} = np2A_o = n(H_o/A_o)\Delta\nu_D 2A_o$$
$$= 2nH_i\Delta\nu_D(A_o/A_i)^{-1}, \tag{4}$$

where we substituted for H_o. The noise is given by the square root of the number of photons underneath the observed line, which for shallow depths H_o is approximately

$$\text{noise} = \sqrt{n2A_o} = \sqrt{2nA_i}(A_o/A_i)^{1/2}. \tag{5}$$

Hence, the S/N for a fixed Doppler shift of $\Delta\nu_D$ is

$$\text{S/N} = \frac{\sqrt{2n}\Delta\nu_D H_i}{\sqrt{A_i}(A_o/A_i)^{3/2}}. \tag{6}$$

Solving for the Doppler shift that produces an S/N of unity,

we find a Doppler velocity error ($\delta V/c = \Delta\nu_D/\nu$) of

$$\delta V_{\text{conv}} = (A_o/A_i)^{3/2} \frac{(c/\nu)\sqrt{A_i}}{\sqrt{2nH_i}} \tag{7}$$

for the conventional technique. (The expression is analogous when angstrom units are substituted for frequency, and λ for ν.) The above is $\sqrt{2}$ smaller than a more exact result for a Gaussian intrinsic line (e.g., eq. [15] in Ge 2002). The important point is that for the conventional method, the velocity noise is proportional to the 3/2 power of the blurring ratio.

4.2. Estimation for the EDI

In estimating the EDI signal, we add a step (Fig. 7*c*) not present for the conventional spectrograph. This is the multiplication of the absorption line by the interferometer comb *prior* to the blurring. In Figure 7*c*, the rectangular absorption line takes a "bite" out of the square wave, removing an area of $H_i\nu_2$, where ν_2 is the relative position of the absorption line to the comb. The comb by itself when completely blurred would produce a continuum of $\frac{1}{2}$. Hence, removing an area of the bite lowers the blurred curve $B(\nu)$ below this continuum by the same area. Thus, the depth of the detected line is $H_o = \text{bite}/A_o = H_i\nu_2/A_o$.

Under a Doppler shift $\nu_2 \rightarrow \nu_2 + \Delta\nu_D$, the dominant but not only effect on $B(\nu)$ is the change in *depth* of the detected line.
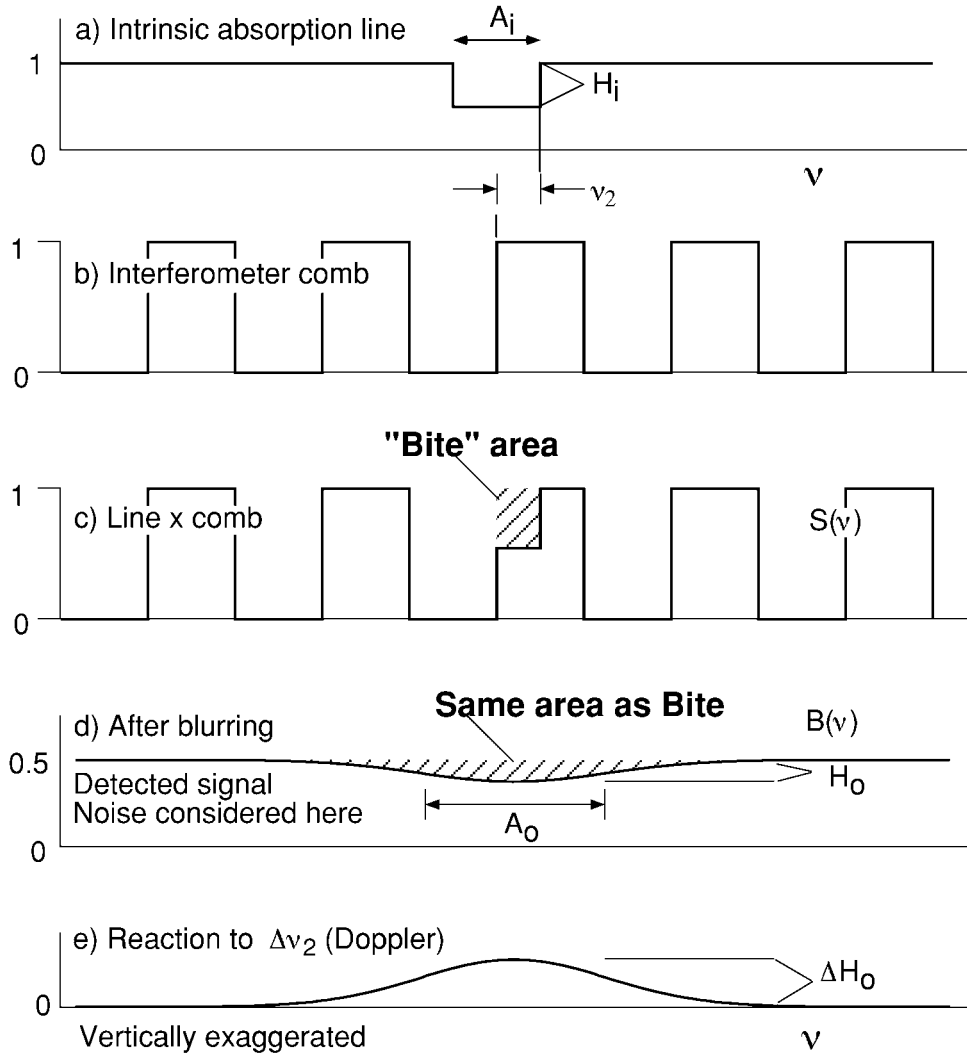
FIG. 7.—Simplified calculation of Doppler reaction function for the EDI. (*a*) Intrinsic absorption line. (*b*) Interferometer comb modeled as square wave. (*c*) The spectrum leaving the interferometer is a product of (*a*) and (*b*). The absorption line takes a "bite" out of one of the fringes, reducing its area (*crosshatched*). (*d*) Detected signal. The interferometer comb is averaged away by blurring. The area of detected line below the continuum is the same as the "Bite" area. The width of the detected line is the same as for the conventional case. (*e*) Reaction function. The dominant effect of Doppler-shifting the absorption line position ν_2 is to change the depth of the detected line.

(The smaller effect is the horizontal shift, as in a conventional spectrograph. This will be ignored here but is considered in the exact calculation later.) Therefore, the reaction function has the same shape as the blurred line in Figure 7*d*, but with height $\Delta H_o = H_i \Delta\nu_D / A_o$ and area $\Delta H_o A_o = H_i \Delta\nu_D$. The signal is this area times the continuum intensity of $n/2$, or

$$\text{signal} = n H_i \Delta\nu_D / 2. \qquad (8)$$

Now let us consider the noise contribution. The width of the EDI blurred absorption line in Figure 7*d* is the same as in the conventional case. Hence, the number of photons underneath is one-half since we have considered only one of two available interferometer outputs so far. Then the noise is

$$\text{noise} = \sqrt{n A_o} = \sqrt{n A_i} (A_o / A_i)^{1/2}, \qquad (9)$$

and the S/N for the single output is

$$\text{S/N} = \frac{\sqrt{n} \Delta\nu_D H_i}{2\sqrt{A_i} (A_o / A_i)^{1/2}}. \qquad (10)$$

Note that the noise comes from the *blurred* signal (Fig. 7*d*) and not the one (Fig. 7*c*) immediately after multiplication by the interferometer comb, where the fringes have a high contrast.

The latter is for the mind's eye only. Hence, the issue of photon noise at the bottom of a dark interferometer fringe is immaterial for this example.

This is a key point that may help the reader understand the EDI operation. The blurring occurs *after* the multiplication of the interferometer comb on the input spectrum. Hence, the fine resolving power of the interferometer comes into play in spite of the lack of resolving power of the spectrograph.

Setting equation (10) to unity solves for the Doppler noise for the EDI, for one output:

$$\delta V_{\mathrm{edi}} = (A_o/A_i)^{1/2} \frac{2(c/\nu)\sqrt{A_i}}{\sqrt{n}H_i}. \tag{11}$$

The complementary interferometer output will produce an identical signal. Supposing we also detect it, the net δV improves by $\sqrt{2}$:

$$\delta V_{\mathrm{edi}} = (A_o/A_i)^{1/2} \frac{\sqrt{2}(c/\nu)\sqrt{A_i}}{\sqrt{n}H_i}. \tag{12}$$

The ratio between the two techniques is

$$\frac{\delta V_{\mathrm{edi}}}{\delta V_{\mathrm{conv}}} = 2(A_o/A_i)^{-1}. \tag{13}$$

Hence, for medium- or low-resolution spectrographs in which $(A_o/A_i) > \sim 2$, $\delta V_{\mathrm{edi}} < \delta V_{\mathrm{conv}}$. Thus, we have demonstrated that the introduction of the interferometer fringes on the spectrum can reduce the photon Doppler velocity noise.

Second, the addition of fringes does not prevent the measurement of the conventional Doppler reaction, the one neglected above, from the same CCD data. Averaging over all phases produces the ordinary spectrum from the fringing spectrum. Provided both interferometer outputs are used so that there is not a significant flux loss by the insertion of the interferometer, the net Doppler S/N will be improved by the inclusion of fringes for all spectrograph resolutions.

5. EXACT CALCULATION FOR A GAUSSIAN LINE

A second, but exact example is of a single Gaussian line using Gaussian spectrograph blurring. A sinusoidal interferometer comb was used repeatedly in four phases spaced 90° apart. (Formal description of B are given by eqs. [21] and [23]). The final reaction function ΔB used in equation (17) was a sum in quadrature

$$\Delta B^2 = \tfrac{1}{4}(\Delta B_0^2 + \Delta B_{90}^2 + \Delta B_{180}^2 + \Delta B_{270}^2) \tag{14}$$

of the separate reactions. The calculation was performed numerically rather than analytically to avoid algebraic errors and to guarantee that identical blurring was applied to both con-

ventional and EDI cases. The only coding distinction in evaluating $B(\nu)$ between the conventional and EDI cases was the multiplication by the interferometer comb prior to blurring.

The following equations were used to convert reaction functions to velocity noise, taken from Connes (1985). In the "detector noise" case, the signal noise is constant and given by the square root of the continuum. In the "shot noise" case (i.e., photon noise), the signal noise depends on the square root of the local intensity. We used

$$\delta V_{\mathrm{detector}} = \frac{(c/\nu)\langle B(\nu)\rangle}{\sqrt{n}\sqrt{\sum \mathrm{DD}^2}}, \tag{15}$$

$$\delta V_{\mathrm{shot}} = \frac{(c/\nu)\sqrt{\langle B(\nu)\rangle}}{\sqrt{n}\sqrt{\sum [\mathrm{DD}^2/B(\nu)]}}, \tag{16}$$

where the sum is over all the pixels of the bandwidth, which encompasses a region much wider than the line, and where the Doppler derivative (DD) is the reaction function per Doppler shift,

$$\mathrm{DD} \equiv \frac{B(\nu, \nu_L + \Delta\nu_{\mathrm{D}}) - B(\nu, \nu_L)}{\Delta\nu_{\mathrm{D}}}, \tag{17}$$

and the second argument in $B(\nu, \nu_L)$ describes the absorption-line position. While for the conventional case $\mathrm{DD} = \partial B/\partial \nu$, for the EDI case $\mathrm{DD} > \partial B/\partial \nu$, because of the interaction of the absorption line against the fine interferometer comb prior to blurring.

Figure 8 shows the velocity noise results evaluated for a single Gaussian line of 50% depth, an FWHM of 0.5 cm^{-1} at 20,000 cm^{-1}, and a fixed input flux of 2.5×10^5 photons cm^{-2} (10^6 photons Å^{-1}) plotted versus the spectrograph blurring ratio (A_o/A_i). The latter is related to the spectrograph resolution R by

$$A_o^2 = A_i^2 + (\nu/R)^2. \tag{18}$$

The detector and shot noise cases are shown as thin and thick curves, respectively. The conventional cases are shown as dashed lines. These vary as $(A_o/A_i)^{3/2}$, confirming equation (7).

The EDI cases are shown as solid curves labeled "EDI-net" and "EDI-fringing only." Equations (14)–(17) produce the EDI-net case, which includes both conventional and EDI effects. This is because equation (17) makes no distinction between the EDI reaction (the change in depth of the detected line) and the conventional reaction (translation along dispersion axis). The "EDI-fringing only" cases are computed by first removing from $B(\nu)$ the ordinary nonfringing spectral variation prior to the computation of DD(ν).

Because the EDI and conventional reactions are orthogonal, we expect their S/Ns $(\propto \delta V^{-1})$ to add in quadrature. Indeed, we
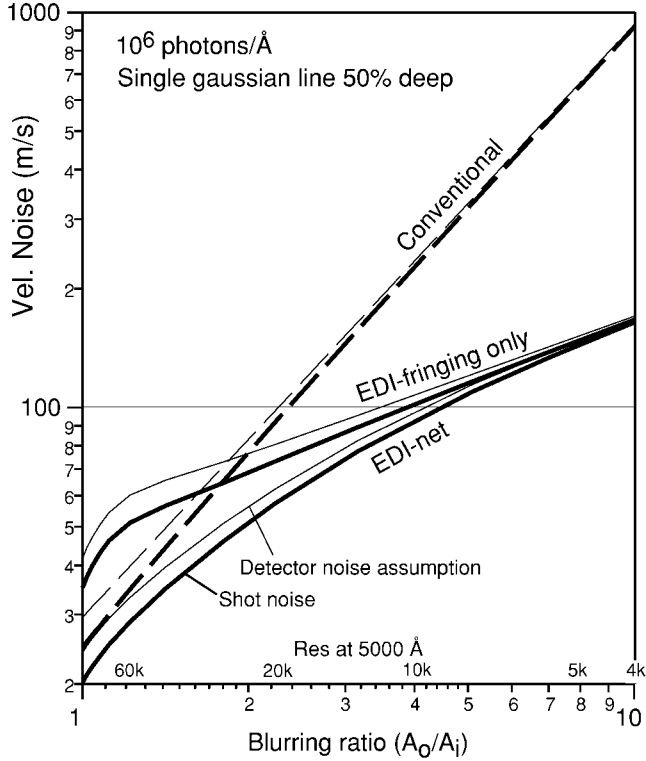
FIG. 8.—Calculated velocity noise for a single Gaussian line receiving 10^6 photons Å^{-1} at 5000 Å in the continuum, for conventional and EDI spectroscopies. The thin curves assume constant noise set by continuum flux. The thick curves assume noise varying as the square root of local intensity. The EDI-net curve includes both fringing and nonfringing components. Both interferometer outputs are used.

find from Figure 8 that

$$\delta V_{\text{edi net}}^{-2} = \delta V_{\text{edi fringe}}^{-2} + \delta V_{\text{conv}}^{-2}. \quad (19)$$

The EDI-fringing only curves vary as $(A_o/A_i)^{1/2}$, confirming equation (12). The EDI approximation method developed by Ge (2002) agrees with this, apart from being a factor of 1.7 lower as the result of a particular choice in assumed line width of the detected signal. Our numerical method (eqs. [14]–[17]) requires no assumption about line width since the summation region broadly encompasses the line.

We find that $\delta V_{\text{edi}} < \delta V_{\text{conv}}$ for medium- or low-resolution spectrographs in which $(A_o/A_i) > 1.8$. For the EDI-net signal, the EDI noise is lower than the conventional for all resolutions.

The analogous calculation for the solar spectrum is similar to the single Gaussian line having a 0.5 cm^{-1} width presented here. The S/N behavior evaluated for actual G and M stellar spectra versus choice of bandwidth, wavelength, τ, and choice between linear and second echelle gratings will be elaborated in a future paper.

6. FOURIER THEORY OF OPERATION

Another explanation for the EDI behavior is presented below. Because the interferometer transmission is sinusoidal, it is natural to use the Fourier domain. Second, the behavior along the frequency dimension (ν) is the most fundamental. The transverse (y) behavior is secondary and implementation-dependent; it merely describes how the phase of the interferometer is encoded, and in the case of phase-uniform data-taking, it is not needed at all.

6.1. Normalized Interferometer Spectral Comb

The ideal interferometer spectral comb is normalized to an average value of unity so that the total number of photons at the detector is the same between the EDI and conventional (grating only) techniques:

$$T'(\nu, y) = 1 + \cos(2\pi\tau\nu + \phi_y). \quad (20)$$

This facilitates comparison of performance per detected photon.

6.2. Lossless Two-Output Operation

In the simple Michelson design used for the prototype, only one output was used, and hence the loss would be 50%. However, a Mach-Zehnder interferometer design would allow both output arms to be directed through the spectrograph and detected on adjacent CCD pixels, ideally producing no net loss. This can also be done with interferometers using polarization to encode the two outputs that travel generally in the same direction, which are eventually split to different pixels at the CCD.

6.3. Conventional Spectroscopy

Let the intrinsic input spectrum (e.g., Fig. 4a) be denoted $S_0(\nu)$, and the PSF (blurring response of the spectrograph for a pure frequency) be denoted PSF (ν). Then in conventional, purely dispersive spectroscopy, the detected signal is

$$B_{\text{conv}}(\nu) = S_0(\nu) \otimes \text{PSF}(\nu). \quad (21)$$

The blurring (convolution) action is more conveniently expressed in the Fourier space, as a straight multiplication:

$$b_{\text{conv}}(\rho) = s_0(\rho)\,\text{psf}(\rho), \quad (22)$$

where the lowercase "psf" denotes the Fourier transform version of the given function.

6.4. Feature Density Distributions

Figure 9a shows the spatial frequencies (ρ) presented to the spectrograph, and Figure 9b the ability to resolve them. The Fourier transform of $S_0(\nu)$ is $s_0(\rho)$, shown as the thin curve. The most important region for Doppler velocimetry is near
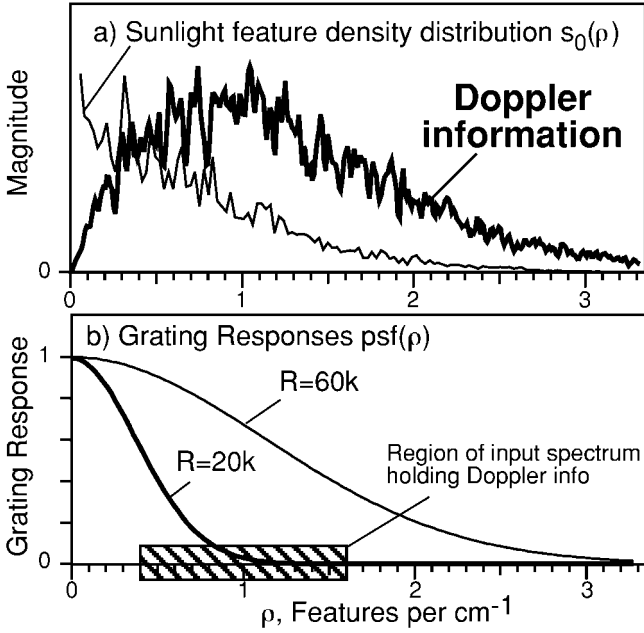
FIG. 9.—(a) Spatial frequencies presented to the spectrograph and (b) the ability to resolve them. (a) Fourier transform $s_0(\rho)$ of solar spectrum (*thin curve*) and its Doppler content $\rho s_0(\rho)$ (*thick curve*), which is its derivative. Vertical units are arbitrary. (b) Gaussian-modeled grating responses psf (ρ) having $R = 60,000$ (*thin curve*) and $R = 20,000$ (*thick curve*). $R = 20,000$ is insufficient to detect the important $\rho \sim 1$ region.

$\rho \sim 1$ cm. This is seen by plotting the derivative of the spectrum $\partial S / \partial \nu$, which in ρ-space is $\rho s_0(\rho)$ (*thick curve*). This curve is proportional to the Doppler information content and has a broad maximum near 1 cm. Thus, a Doppler velocimeter should be sensitive to the $\rho \sim 1$ cm region.

Figure 9b shows the ability of the conventional instrument to resolve the spatial frequencies. The psf (ρ) is analogous to a modulation transfer function. Gaussian-modeled grating responses having $R = 60,000$ and $R = 20,000$ are shown. The narrow $R = 20,000$ peak is insufficient to detect the important $\rho \sim 1$ region.

6.5. EDI Spectroscopy

The passage of light through the interferometer multiplies the spectral comb $T(\nu)$ against the spectrum *prior* to the blurring action of the external grating spectrograph. Hence, the EDI-detected signal is

$$B_{\text{edi}}(\nu) = [S_0(\nu)T'(\nu)] \otimes \text{PSF}(\nu), \qquad (23)$$

which becomes a sum of the ordinary spectrum plus the new

fringing components

$$B_{\text{edi}}(\nu) = B_{\text{conv}}(\nu) + \tfrac{1}{2}[S_0(\nu)e^{i\phi_y}e^{i2\pi\tau\nu}$$
$$+ S_0(\nu)e^{-i\phi_y}e^{-i2\pi\tau\nu}] \otimes \text{PSF}(\nu). \qquad (24)$$

In Fourier space, this is

$$b_{\text{edi}}(\rho) = b_{\text{conv}}(\rho) + \tfrac{1}{2}e^{i\phi_y}s_0(\rho + \tau) \, \text{psf}(\rho)$$
$$+ \tfrac{1}{2}e^{-i\phi_y}s_0(\rho - \tau) \, \text{psf}(\rho), \qquad (25)$$

where we used the well-known property of Fourier transforms that, multiplied by a phasor $e^{i2\pi\tau\nu}$, shifts the conjugate Fourier variable ρ (by amount τ). The result consists of the ordinary detected signal b_{conv} plus two fringing terms that counterrotate in the complex plane versus ϕ_y.

6.6. Conversion to a Vector Spectrum: Whirl

The purpose of measuring the fringing spectrum at multiple phase outputs (ϕ_y) is to isolate one of these two fringing components so that the Doppler effect rotates the signal in one direction only. This allows a simple vector based the interpretation of the Doppler effect through dot products (§ 8).

The scalar spectrum is converted to a vector spectrum (a complex wave) called a "whirl" in a kind of phase-stepping process. We will discuss the phase-slanted mode. Since ϕ_y varies versus y, one can combine $I(\nu)$ from different y-channels in a linear combination analogous to the four-bucket algorithm described in Greivenkamp & Bruning (1992) but using complex weightings. For clarity, let us bin the interferometer outputs into four components separated by $\Delta\phi_y = 90°$ intervals, and let us designate these as B_0, B_{90}, B_ϕ, etc. (An equation using three components at a 120° separation is equally valid but less elegant in appearance.) Then we form a "whirl" by linear combination, using a prefactor of $\tfrac{1}{4}$ so that the total flux is the same as in a single exposure:

$$W(\nu) = \tfrac{1}{4}[(B_0 - B_{180}) + i(B_{90} - B_{270})]. \qquad (26)$$

(Eq. [26] is related to the more general form in eq. [52] discussed in § 8.3.) This linear combination eliminates the non-fringing component $B_{\text{conv}}(\nu)$ because it does not vary with ϕ_y. It also eliminates one of the two counterrotating fringing terms.

6.7. Formation of Moiré Fringes

Applying equation (26) to equation (25), we get the whirl in Fourier space:

$$w(\rho) = \tfrac{1}{2}s_0(\rho + \tau) \, \text{psf}(\rho). \qquad (27)$$

This important equation describes the formation of the moiré

fringes. The argument in $s_0(\rho + \tau)$ shows that the input spectrum is shifted (heterodyned) in ρ-space.

These actions are illustrated in Figure 10. Figure 10a shows the input spatial frequency distribution $s_0(\rho)$. The regions at $\rho \sim \pm 1$ cm important for Doppler velocimetry are blackened. Figure 10b shows $s_0(\rho)$ shifted by τ after interaction with the interferometer.

Figure 10c shows the detected signal after blurring by psf (ρ). Only the low-ρ portions survive. These are the moiré fringes expressed in Fourier space. Heterodyning allows the EDI to use lower R and still detect the blackened region important for velocimetry. The slanted spectral comb seen faintly in the measured data (Figs. 5a and 5b) is the remnant of the continuum spike, now shifted to $\rho = -1$ cm.

6.8. Nonfringing Spectrum

The ordinary (nonfringing) spectrum can be obtained from a set of fringing spectra by vector addition so that the fringing terms cancel:

$$B(\nu) = \tfrac{1}{4}(B_0 + B_{180} + B_{90} + B_{270}). \qquad (28)$$

The nonfringing spectrum from the same EDI data set can be processed for Doppler velocity in the conventional manner (Butler et al. 1996) and its result averaged with the EDI velocity. Due to the heterodyning, the nonfringing and fringing information occupy different spatial frequencies in the CCD data and hence are independent. Thus, the combined EDI-conventional photon S/N is always better than the conventional instrument alone.

6.9. Effective Instrument Response

The heterodyning changes the ρ between input and output. For comparing techniques, it is useful to describe the effective instrument response by the ρ of the input (rather than of the detected signal as in Fig. 10c). By changing variables $\rho \rightarrow (\rho - \tau)$, equation (27) becomes

$$w(\rho - \tau) = \tfrac{1}{2}s_0(\rho)\, \mathrm{psf}\,(\rho - \tau). \qquad (29)$$

This shows the grating response psf (ρ) shifted toward higher ρ by τ and reduced in amplitude by half. We summarize the effective responses for the two techniques, using the *same* grating:

$$\mathrm{psf}_{\mathrm{conv}} = \mathrm{psf}_0\,(\rho), \qquad (30)$$

$$\mathrm{psf}_{\mathrm{edi}} = \tfrac{1}{2}\gamma\,\mathrm{psf}_0\,(\rho - \tau), \qquad (31)$$

where γ is the interferometer visibility, which is unity in the ideal case. Figure 11 illustrates how heterodyning shifts the
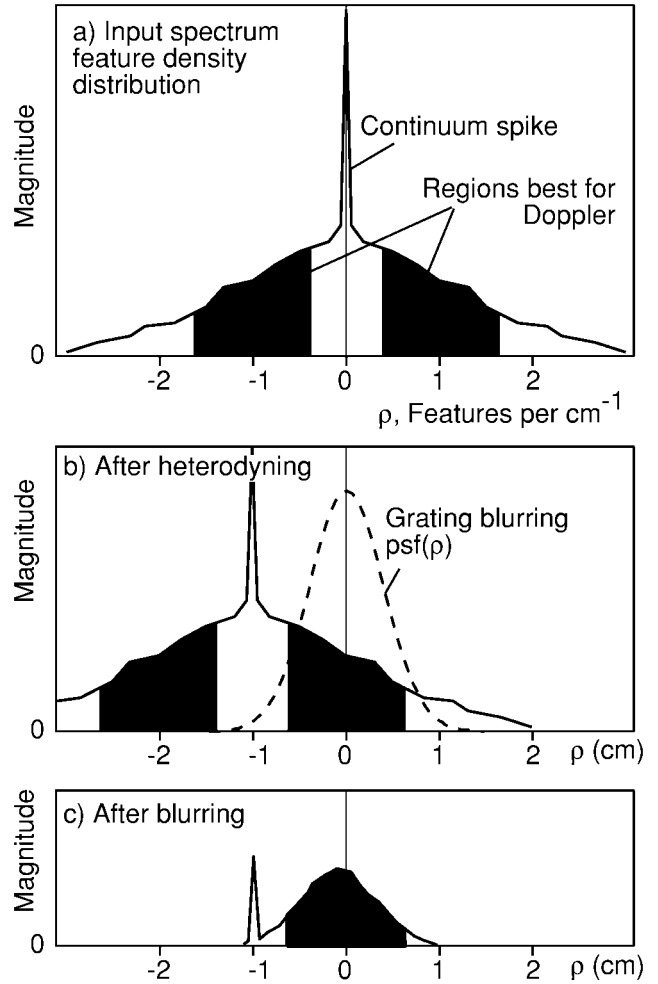

FIG. 10.—Stages in heterodyning process, in Fourier space. (*a*) Input $s_0(\rho)$. The regions near $\rho \sim \pm 1$ cm hold the most Doppler information and are blackened for labeling. (*b*) After passage through the interferometer, $s_0(\rho)$ shifts by $\Delta\rho = \tau$. This places a blackened regions near the origin where it better survives the grating blurring psf (ρ) (*dashed curve*). (*c*) The data near the origin expresses the moiré fringe. The continuum spike remnant, now shifted to $\rho \sim -1$ cm, corresponds to the sinusoidal comb faintly seen in the CCD data (Figs. 5a and 5b).

EDI response over the most important region for Doppler velocimetry.

6.9.1. Relative Doppler Sensitivity

The height of the curves in Figure 11 is proportional to the photon S/N, for a given region of ρ. This is because continuum noise manifests the same level (uniform vs. ρ) for both techniques. The area under the EDI peak for $R = 20{,}000$ is about $\tfrac{1}{2}$ the area under the conventional $R = 60{,}000$ curve for $\rho \sim 1$ cm. Hence, $\mathrm{S/N}_{\mathrm{edi}}(R = 20{,}000) \sim (1/2)\mathrm{S/N}_{\mathrm{conv}}(R = 60{,}000)$. This is confirmed by Figure 8 as well as by an exact calculation using the solar spectrum.
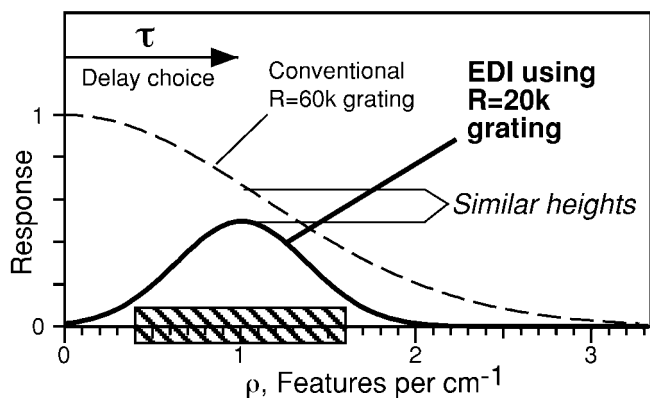
FIG. 11.—The interferometer shifts the grating response to higher ρ by $\Delta\rho = \tau$. The EDI response using $R = 20,000$ is comparable to that of the $R = 60,000$ grating (*dashed curve*) in the important $\rho \sim 1$ cm region. The photon S/N is proportional to the altitude of the curves.

6.9.2. Robustness against PSF Drifts

Velocimeter performance is often limited by instrumental noise, such as beam shape or grating PSF variations, rather than photon noise. The EDI is dramatically more resistant to such errors because of the interferometer comb, which acts as a fiducial net. Drifts in the PSF affect the comb $T(\nu)$ the same way as $S_0(\nu)$. Figure 12 shows an equivalent explanation in Fourier space.

7. THE DOPPLER EFFECT

7.1. EDI Moiré Fringe Rotation

For a nonrelativistic velocity V, the frequency scales under the Doppler effect as $\nu \rightarrow (1 + V/c)\nu$, so that for over a limited bandwidth there appears to be a shift

$$\Delta\nu_D = (\Delta V/c)\nu, \qquad (32)$$

where c is the speed of light. The EDI Doppler measurement uses the change in moiré phase. The moiré pattern is described by the whirl:

$$W(\nu) = \tfrac{1}{2}[e^{i2\pi\tau\nu}S_0(\nu)] \otimes \mathrm{PSF}(\nu), \qquad (33)$$

which is from equation (27). Under a Doppler shift $\nu \rightarrow \nu + \Delta\nu$, the phasor $e^{i2\pi\tau(\nu+\Delta\nu_D)}$ causes the whirl to rotate in the complex plane

$$W_1(\nu) = W_0(\nu)e^{i2\pi\tau\Delta\nu_D} \qquad (34)$$

by an angle $\theta = \tau\Delta\nu_D$ in cycles, fringes, or revolutions. (Over wide bandwidths, the rotation is a twist because of the slowly changing ν.)

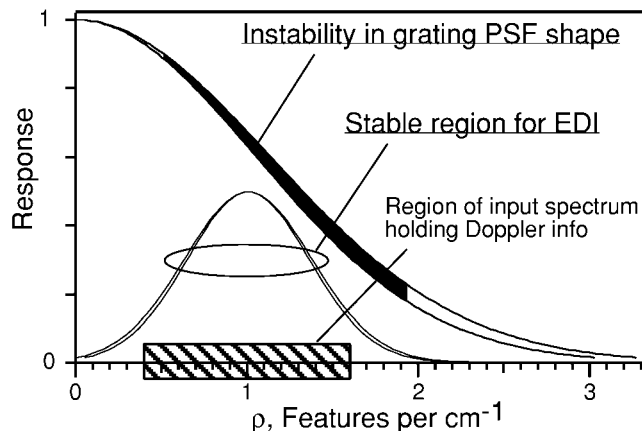We make a simultaneous measurement of both the solar and

FIG. 12.—Effect of grating PSF fluctuations, in Fourier space. The changes at $\rho \sim 1$ cm are much larger for the conventional technique than for the EDI technique. The top of the EDI peak is the most stable, and this is optimally placed over the most important region for velocimetry.

reference (iodine) spectra, and thus the same value of τ applies to each. Since the Doppler velocity is a difference between those two components, we can ignore small drifts in τ.

7.2. Velocity per Fringe Proportionality

Changing $\tau\Delta\nu_D$ in equation (34) by unity corresponds to one revolution of whirl rotation. Hence,

$$\Delta V = \Delta\theta\mathrm{VPF}, \qquad (35)$$

$$\mathrm{VPF} = (\lambda/\tau)c, \qquad (36)$$

where the velocity per fringe (VPF) proportionality for our experimental parameters is ~ 14 km s^{-1} per fringe.

Equation (34) neglects the minor wavelength dependence of the refractive index of the glass slab in the interferometer (Barker & Schuler 1974). Counting the number N_F of interferometer fringes seen in white-light fringing spectra versus ν automatically includes this. Then $\tau = \Delta N_F/\Delta\nu$. Another issue is what to use for λ, since the distribution of lines may not be uniform across the band. Calibrating the EDI by the Earth's rotation in sunlight or starlight is best since it automatically includes all the above effects.

8. DATA ANALYSIS

Equation (26) is useful for formal analysis, but the whirl may be formed from the phase-slanted CCD intensity data $I(\nu, y)$ by a mathematically equivalent method. This uses all the y-channels, not requiring them to be spaced every 90°. The CCD data are organized into vertical lineouts $I_\nu(y)$. The average period P_y along y is found. The Fourier amplitudes of $I(\lambda)$ are

found by multiplying against a sine or cosine wave of P_y and summing over y-pixels. The resulting cosine and sine Fourier amplitudes $F_{y,c}$ and $F_{y,s}$ are assigned to the real and imaginary parts of W for that ν-channel:

$$W \propto F_{y,c} + iF_{y,s}. \tag{37}$$

Alternatively, $I(y)$ can be fitted to a fixed-period sinusoid with the resulting phase and amplitude assigned to W in polar coordinates; then W is converted to rectangular coordinates.

8.1. Dot Products

The whirl rotation is determined by performing a dot product (overlap integral) of the data against template whirls. The dot product between two whirls (W, U) is the per channel dot product summed or averaged over all ν-channels:

$$W(\nu) \cdot U(\nu) \equiv \sum_{\nu} W_{\mathrm{Re}}U_{\mathrm{Re}} + W_{\mathrm{Im}}U_{\mathrm{Im}}, \tag{38}$$

where Re and Im denote real and imaginary parts, respectively. The order of the summation is immaterial. This implies that for velocimetry it does not matter that the pixels are not linear in ν (e.g., realistic spectrographs). From any whirl W, we can create a perpendicular whirl $W_\perp$ by exchanging the real and imaginary parts and inverting one of them:

$$W_\perp \equiv iW = -W_{\mathrm{Im}} + iW_{\mathrm{Re}}, \tag{39}$$

so that $W \cdot W_\perp \equiv 0$.

Let U be some template whirl that defines the zero angle. This could be a measured whirl at a designated time zero. Then a rotated whirl is

$$W = aU + a_\perp U_\perp, \tag{40}$$

with scalar coefficients a and $a_\perp$. These are found by dotting U and then $U_\perp$ against equation (40) and utilizing the orthogonality. This yields

$$\tan\theta = \frac{a_\perp}{a} = \frac{W \cdot U_\perp}{W \cdot U}. \tag{41}$$

Implicit in equation (41) is that the arctangent function is taken *after* the dot product has been averaged over all ν-channels, rather than calculating $\theta(\nu)$ before averaging. This solves the problem existing in regions between major spectral lines where small fringe visibility would cause $\theta(\nu)$ to vary wildly under noise.

8.2. Decomposition of a Composite Whirl

For each velocity datum, we measure the stellar spectrum through the iodine vapor cell. We presume that the resulting "Stellio" whirl contains both stellar (U) and iodine (V) com-ponents:

$$W = U + V. \tag{42}$$

(This is a small signal approximation for absorptive references since absorption is a multiplicative and not additive effect.)

Due to the large number of lines in each whirl component having unrelated phase and position, U and V are almost orthogonal. That is, the "cross talk" is small:

$$\frac{V \cdot U}{\sqrt{(V \cdot V)(U \cdot U)}} \ll 1. \tag{43}$$

For the case of a 130 Å bandwidth in the green, the cross talk is 0.018. The cross talk will further decrease for an increasing bandwidth as more unrelated lines are included. It is not necessary to have perfect orthogonality because the cross talk is included in the linear equations below.

For each Stellio whirl,

$$W = aV + a_\perp V_\perp + bU + b_\perp U_\perp. \tag{44}$$

Against equation (44), we dot-multiply V, $V_\perp$, U, and $U_\perp$, to create four equations:

$$m_v = k_4 a + 0 + k_1 b + k_2 b_\perp,$$
$$m_{v,p} = 0 + k_4 a_\perp - k_2 b + k_1 b_\perp,$$
$$m_u = k_1 a - k_2 a_\perp + k_3 b + 0,$$
$$m_{u,p} = k_2 a + k_1 a_\perp + 0 + k_3 b_\perp. \tag{45}$$

The four coefficients a, $a_\perp$, b, and $b_\perp$ are solved by determinants, using the following constants:

$$k_1 = V \cdot U,$$
$$k_2 = V \cdot U_\perp = -V_\perp \cdot U,$$
$$k_3 = U \cdot U,$$
$$k_4 = V \cdot V, \tag{46}$$

which need only be calculated once, and

$$m_v = V \cdot W,$$
$$m_{v,p} = V_\perp \cdot W,$$
$$m_u = U \cdot W,$$
$$m_{u,p} = U_\perp \cdot W, \tag{47}$$

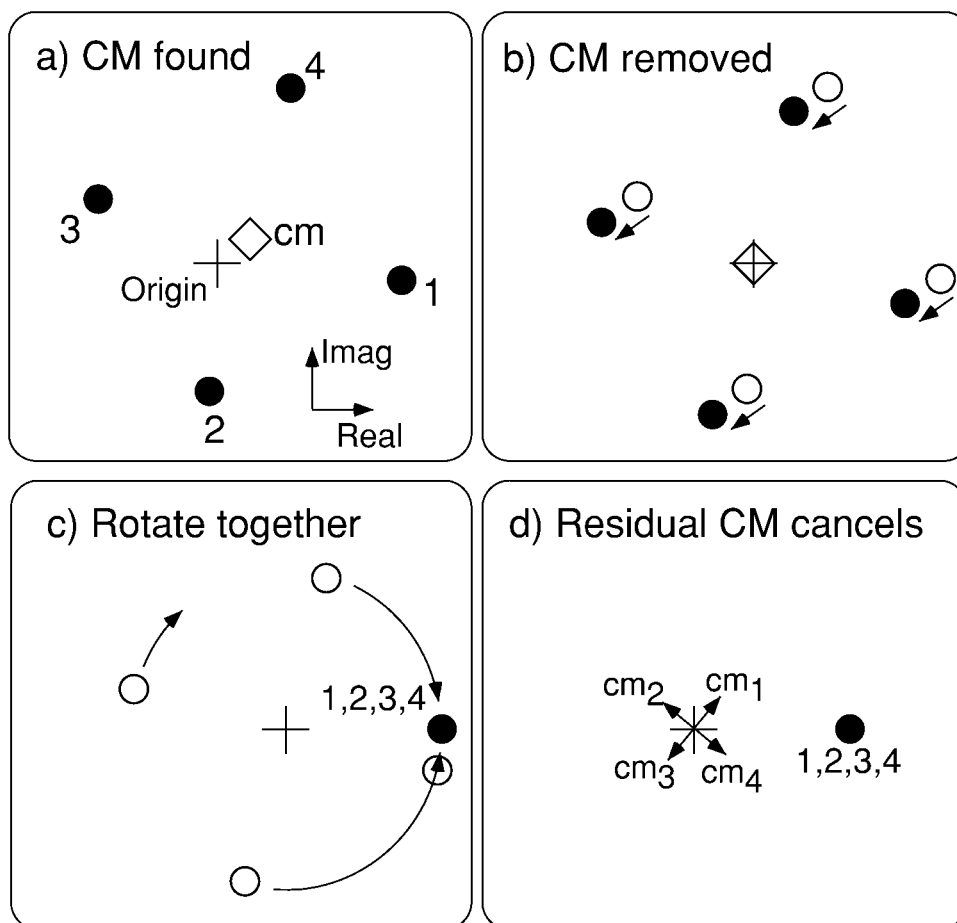which are calculated for each instance. Then θ_v and θ_u are

FIG. 13.—Steps in removing CM error by piston phase stepping, which is a kind of in situ flat-fielding important for reducing instrument noise.

calculated from

$$\tan \theta_v = \frac{a_\perp}{a}; \quad \tan \theta_u = \frac{b_\perp}{b}. \tag{48}$$

The Doppler velocity is the difference $\theta_D = \theta_u - \theta_v +$ const, scaled by VPF (eq. [36]). Since const is unknown at this high level of precision, we measure velocity changes

$$\Delta V = (\Delta\theta_u - \Delta\theta_v)\text{VPF} \tag{49}$$

relative to the first datum or other standard.

8.3. Piston Phase Stepping

A piston phase-stepping (PPS) procedure can be used as a kind of real-time flat-fielding to dramatically reduce-fixed pattern or common mode (CM) errors. Such errors can produce significant instrument velocity noise. Examples are CCD pixel-to-pixel gain variations and a parasitic interference from window reflections that create a false appearance of fringes. The advantage of PPS is that it is in situ—it occurs at the actual time and optical configuration of stellar data-taking, so the apparatus is not changed to use a different source as in traditional flat-fielding.

In PPS, ϕ_y is incremented by $\Delta\phi_p$ for all y-positions by the PZT transducer (Fig. 1) on which one of the mirrors is mounted. In equation (3) for ϕ_y, n is the step index for the set of exposures used to compute an averaged whirl. The steps should be evenly distributed about the phase circle so that their vector sum is zero. Then the N_p multiple exposures are averaged together after appropriate rotation to form a coherently averaged or push-pull whirl ($W_{\text{p-p}}$).

Figure 13 illustrates the three-step process. (1) The whirl describing the CM error is found by vector-summing the singlet whirls without rotation (Fig. 13a):

$$\mathbf{CM} = \frac{1}{N_p} \sum_n W_n. \tag{50}$$
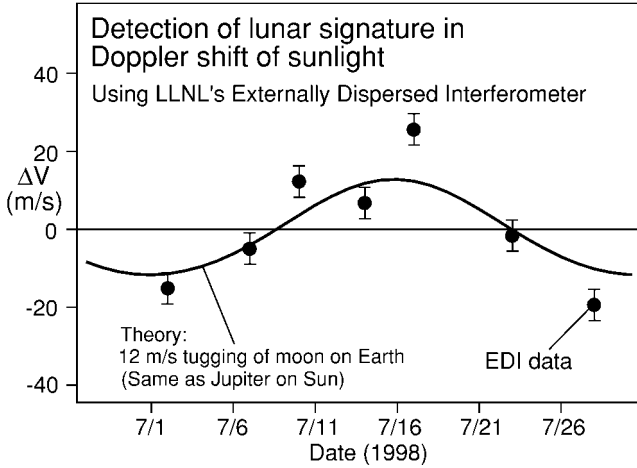
(2) The CM is subtracted from every singlet whirl to form

FIG. 14.—Early EDI prototype, which detected the 12 m s^{-1} amplitude Doppler signature of the Moon tugging the Earth. Sunlight fringing spectra were measured, and the effects of the Earth's orbit and daily rotation subtracted, leaving the wobble caused by the Moon's gravitational pull. This is the same size effect as a Jupiter-like planet pulling a star. The 8 m s^{-1} scatter is believed due to a pointing error of the rooftop heliostat against the 4000 m s^{-1} velocity gradient of the solar disk. The ± 4 m s^{-1} error bars show long-term instrument error estimated from bromine-iodine tests lacking the heliostat error.

cleaned whirls (Fig. 13b):

$$W_n' = W_n - \mathbf{CM}. \tag{51}$$

(3) Finally, the cleaned whirls are coherently averaged to form the push-pulled whirl (Fig. 13c):

$$W_{\text{p-p}} = \frac{1}{N_p} \sum_n W_n' e^{-in\Delta\phi_P}, \tag{52}$$

where the whirls are first counterrotated by the piston phase step so that they reinforce rather than cancel each other. This also cancels any residual CM error that survives step 1 (Fig. 13d).

Note the mathematical similarity between the counterrotating process here and that in the y-dependent phase stepping (eq. [26]) used to form the whirl from phase-slanted fringes. Both strive to cancel certain components by strategically chosen rotations.

9. EDI LAB PROTOTYPE

Figure 1 diagrams the first implementation of the EDI, proposed and built in 1997–1998 by the author for lab testing on sunlight and the bromine vapor spectrum. The ~1 m apparatus size was set by the Jobin-Yvon 640 spectrograph since the interferometer was only ~10 cm in size. Most components were inexpensive and readily available in a standard optics lab, already on hand, or commercially available off-the-shelf. The design and data-taking procedure details are similar to those

described in the companion paper (Ge et al. 2002) used in first light stellar measurements at the Lick Observatory 1 m telescope in 1999. The interferometer was of an angle-independent design (Hilliard & Shepherd 1966) in order to produce the best fringe visibility for extended sources such as optical fiber bundles, spectral lamps, or blurry star images.

This prototype was for proof of the principle demonstrations of the EDI concept. For expediency, the optics were mounted in the open air without convective housing or environmental controls, and lacking stabilization for the interferometer cavity length (cavity drifts <λ/3 over the 15 s exposures were manageable). These kinds of controls would be expected in a mature installation.

No means for converting the round input beam shape to a narrow rectangle was employed. Consequently, most photons were lost at the slit, so bright sources were required. These included sunlight and bromine vapor backlit by white light. The latter is a convenient bright and multiline absorption spectrum useful for testing measurement repeatability without heliostat-induced velocity errors or the 5 minute oscillations of the photosphere. The bromine repeatability tests are described in Erskine & Ge (2000) and Ge et al. (2002). These tests showed a short-term instrument noise as low as 0.76 m s^{-1} (corresponding to a λ/18,000 white-light fringe shift), and the zero-point drifts over 11 days were not more than 4 m s^{-1}.

9.1. Lunar Signature Seen in Sunlight

Sunlight tests showed that the EDI can detect the rotation of the Earth, the 12 m s^{-1} lunar signature component in the Earth's orbit, and zero-point drifts over 1 month not more than a few meters per second. A heliostat/lens on the roof focused sunlight into a 0.6 mm diameter fiber conducting light to the instrument in the lab. Four 15 s exposures were made while the interferometer phase was stepped in ~90° increments. Each velocity datum plotted in Figure 14 represents ~1 minute of exposure time. The exposures were made at different hours of the day and 7 different days of the month in 1998 July (the raw data were unanalyzed until recently and hence were not discussed in earlier papers).

The diurnal acceleration of the Earth due to its rotation was clearly seen in a range of velocities over 400 m s^{-1} wide over a 5 hr interval. This proved that the effect measured by the EDI instrument and interpreted by the novel vector data analysis (§ 8) was indeed a Doppler effect.

After theoretical diurnal and annual orbital motion components were subtracted, the residual velocity component (Fig. 14) was consistent with the lunar component. Essentially, we detected the Moon tugging the Earth at 12 m s^{-1} amplitude.

This is a relevant test because it is the same amplitude as Jupiter tugging the Sun (although at a 1 month period not 12 yr). This demonstrated that long-term drifts were sufficiently low, even for the prototype without environmental controls, for the EDI to be useful in detecting many planetary Doppler sig-

natures. These are often of a few days period and many tens of meters per second in amplitude.

The 8 m s^{-1} observed scatter in the data about the lunar curve (Fig. 14) is attributed to a previously observed sensitivity of the velocity to the heliostat pointing direction and not to the EDI. Sunlight was semifocused into the fiber end, so that any uneven intensity averaging over the 4000 m s^{-1} rotational velocity gradient across the solar disk produces a velocity offset. This error source would not be present in stellar observations—stellar disks are unresolved. The photon noise estimated for these data is less than 1 m s^{-1} and hence is not significant. (approximately 12×10^9 photons per datum were used). Since the experimental conditions and intensities for sunlight were similar to the bromine tests, the EDI apparatus most likely contributed a similar amount of instrument error, measured at ∼4 m s^{-1}. Hence, we used this value for the error bars of Figure 14, representing the estimated instrumental performance without the heliostat.

9.2. Other Applications of the EDI

While the scope of this paper is limited to Doppler velocimetry, there are several other useful applications of EDI, including the boosting of the effective resolution of a grating spectrograph in mapping a spectrum. The heterodyning that occurs optically is reversed numerically during data analysis, allowing detection of narrow features beyond the normal resolution limit of the spectrograph. The effective resolution of the grating can be boosted 2–3 times while maintaining the original slit width (Erskine & Edelstein 2003a).

Another metrology application is the precision measurement of white-light fringe shifts to measure secondary phenomena that affect the interferometer cavity length (i.e., temperature, acceleration), without danger of fringe skips that come from monochromatic sources (Erskine 2002). Furthermore, if interferometer is a long-baseline interferometer, then fringe shifts measure angles. Dispersing the light allows multiple objects to be observed simultaneously. This produces a differential astrometry measurement that dramatically relaxes the usually restrictive path length stability requirement (Erskine & Edelstein 2003b).

REFERENCES

Barker, L., & Schuler, K. 1974, J. Appl. Phys., 45, 3692
Born, M., & Wolf, E. 1980, Principles of Optics (6th ed.; Oxford: Pergammon)
Butler, R., Marcy, G., Williams, E., McCarthy, C., Dosanjh, P., & Vogt, S. 1996, PASP, 108, 500
Cochran, W., Hatzes, A., Butler, R., & Marcy, G. 1997, ApJ, 483, 457
Connes, P. 1985, Ap&SS, 110, 211
Cumming, A., Marcy, G., & Butler, R. 1999, ApJ, 526, 890
Douglas, N. 1997, PASP, 109, 151
Erskine, D. 2000, Single and Double Superimposing Interferometer Systems. US Patent Number 6,115,121, filed 1997 October 31 and issued 2000 September 5
———. 2002, Combined Dispersive/Interference Spectroscopy for Producing a Vector Spectrum. US Patent Number 6,351,307, filed 2000 February 23 and issued 2002 February 26
Erskine, D., & Edelstein, J. 2003a, Proc. SPIE, in press
———. 2003b, Proc. SPIE, in press
Erskine, D., & Ge, J. 2000, in ASP Conf. Ser. 195, Imaging the Universe in Three Dimensions: Astrophysics with Advanced Multi-Wavelength Imaging Devices, ed. W. van Breugel & J. Bland-Hawthorn (San Francisco: ASP), 501
Frandsen, S., Douglas, N., & Butcher, H. 1993, A&A, 279, 310

Ge, J. 2002, ApJ, 571, L165
Ge, J., Erskine, D., & Rushford, M. 2002, PASP, 114, 1016
Greivenkamp, J., & Bruning, J. 1992, in Optical Shop Testing, ed. D. Malacara (2d ed.; New York: Wiley), 501
Harlander, J., Reynolds, R., & Roesler, F. 1992, ApJ, 396, 730
Harvey, J., et al. 1995, in ASP Conf. Ser. 76, GONG '94: Helio- and Astro-Seismology from the Earth and Space, ed. R. K. Ulrich, E. J. Rhodes, & W. Däppen (San Francisco: ASP), 432
Hilliard, R., & Shepherd, G. 1966, J. Opt. Soc. Am., 56, 362
Kozhevatov, I. E., Kulikova, E. H., & Cheragin, N. P. 1996, Sol. Phys., 168, 251
Marcy, G., & Butler, R. 1996, ApJ, 464, L147
———. 2000, PASP, 112, 137
Mayor, M., & Queloz, D. 1995, Nature, 378, 355
McMillan, R., Moore, T., Perry, M., & Smith, P. 1993, ApJ, 403, 801
Noyes, R. W., Jha, S., Korzennik, S. G., Krockenberger, M., Nisenson, P., Brown, T. M., Kennelly, E. J., & Horner, S. D. 1997, ApJ, 483, L111
Title A., & Ramsey, H. 1980, Appl. Opt., 19, 2046
Vogt, S. 1987, PASP, 99, 1214
Vogt, S., Marcy, G., Butler, R., & Apps, K. 2000, ApJ, 536, 902
Vogt, S., et al. 1994, Proc. SPIE, 2198, 362